Sublimation and deposition in gaseous mixtures

Alexey Ph Polikarpov, Irina Martin Graur, Felix Sharipov

Sublimation and deposition in gaseous mixtures

Alexey Polikarpov[1], Irina Graur[2], Felix Sharipov[3]

[1] *Ural Federal University, 51 str. Lenina, 620000 Ekaterinbourg, Russia*

[2] *Aix-Marseille Université, CNRS, IUSTI UMR 7343, 5 rue E. Fermi, 13453, Marseille, France*

[3] *Departamento de Física, Universidade Federal do Paraná, Caixa Postal 19044, Curitiba, 81531-990, Brazil*

Abstract

The sublimation and deposition behaviors of the Helium-Argon mixture is analyzed numerically in the temperature range where Helium is only in gaseous state while Argon can sublimate and deposit on its own solid phase. The McCormack model is implemented to model the Boltzmann collision term. Three kinds of potential are used for simulation of the intermolecular collisions: Hard Sphere, Lennard-Jones potential, and *ab initio*. The matrices of the kinetic coefficients have been obtained for different values of the rarefaction parameters and molar fraction of non-sublimating gas. The influence of the intermolecular potential on the kinetic coefficients as well as on the gas macroscopic profiles has been analyzed.

1. Introduction

The sublimation and deposition processes are very important in many different natural phenomena and industrial fields. To develop efficient systems of weather and avalanche forecasting, the information about the rate of the atmospheric water vapor deposition onto snow surface and of the snow sublimation is needed [1, 2]. The exploration of particularities of the solar system and especially of the evolution in time of the climatical conditions on the planets requires the development of the model which allows to estimate the rate of mass loss from

Email addresses: alexey.polikarpov@gmail.com (Alexey Polikarpov[1]), irina.martin@univ-amu.fr (Irina Graur[2]), sharipov@fisica.ufpr.br (Felix Sharipov[3])

ice in a planet atmosphere [3]. The solar controlled sublimation of ice has been accepted as the key process governing the cometary activity [4]. The key for the explanation of most phenomena associated with the activity of comets is a proper understanding of the processes taking place within a thin layer around the nucleus/coma interface [5, 6]. Heat and mass transfer at sublimation of solid particles is important in the development of new technologies of chemical vapor deposition [7, 8]. For intensifying and optimizing the operation modes for the low-temperature drying of pharmaceutical and food products the knowledge about the sublimation-deposition phenomena are also indispensable [9, 10].

The simulations of the sublimation and deposition phenomena are essentially restricted to the continuum modeling. However, the evaporation and condensation phenomena, analogous to the sublimation and deposition, have been intensively simulated using the gas kinetic theory. For single-component systems consisting of a pure vapor and its condensed phase, many successful results have been obtained and the summary of them can be found in Ref. [11]. The case of a gas mixture of a vapor and a non-condensable gas was also actively studied in the series of papers. Several kinetic models were applied to mimic the Boltzmann collision operator in case of evaporation and condensation in mixtures, for instance, the Hamel model [12] in Ref. [13], the Carzó-Santos-Brey model [14] in Refs. [15], and the new kinetic model proposed in Ref. [16]. The full Boltzmann collision operator was used for the same purpose in Ref. [17]. Four main geometries were considered: two parallel condensed surfaces [17], half-space problem (one surface) [18], two coaxial cylinders [19, 20], and evaporation from a sphere into surrounding mixture [13, 21]. The particularities of the continuum limit approximation and specific phenomena appearing there, like ghost effect, were also largely discussed in Refs. [22, 19, 20]. However, in

most of these work the hypothetical molecular masses and hard sphere potential with hypothetical diameters were used.

Like evaporation and condensation, the sublimation and deposition phenomena can be also described on the basis of the kinetic theory. In the present paper, we develop a methodology based on the numerical solution of the Boltzmann type kinetic equation to simulate the sublimation-deposition processes. In practice, the sublimation and depositions happen in a gas mixture, where the presence of some amount of gas, which can neither sublimate nor deposit, could affect the whole process. Therefore, the mixture of Helium with Argon was chosen for the specific temperature range, where Helium is being only in a gaseous state while Argon can sublimate and deposit. An experimentally obtained dependency of the saturation pressure on the temperature [23] is used for the chosen temperature range. In order to investigate the influence of the intermolecular potential on mass and heat transfer through the mixture in question, three potentials, namely, the Hard Sphere (HS), Lennard-Jones (LJ), and *ab initio* (AI) [24], are used to describe the intermolecular collisions. The corresponding numerical results are analysed and compared between them.

2. Problem statement

Let us consider a mixture of the monatomic gases, Helium and Argon, confined between two parallel infinite solid layers of Argon separated by a distance H. One component of this mixture, Helium, referred in the following with subscript 1, is completely reflected from the solid surface. The other component of the mixture, Argon, subscript 2, represents the gaseous phase of the solid surfaces so that it can sublimate or deposit (de-sublimate).

The lower solid surface is maintained at the temperature $T_L = T_0 - \Delta T/2$, and located at $y' = -H/2$, while the upper one is kept at the temperature

$T_U = T_0 + \Delta T/2$ and located at $y' = H/2$, where T_0 is the equilibrium temperature, ΔT is the temperature difference between the surfaces, which is small in comparison with the equilibrium temperature, *i.e.*, $\Delta T \ll T_0$. The equilibrium molar fraction of Helium, C_0, is defined as:

$$C_0 = \frac{n_{01}}{n_0}, \qquad n_0 = n_{01} + n_{02}, \tag{1}$$

where $n_{0\alpha}$ is the equilibrium number density of species α ($\alpha = 1, 2$). The equilibrium number density of the mixture, n_0, is related to the equilibrium pressure, p_0, through equation of state $p_0 = n_0 k_{\text{B}} T_0$, where k_{B} is the Boltzmann constant.

The gas rarefaction is characterized by the rarefaction parameter defined as

$$\delta = \frac{H}{\ell}, \qquad \ell = \frac{\mu v_0}{p_0}, \tag{2}$$

where ℓ is the equivalent free path [25], μ is the mixture viscosity [24] at the equilibrium temperature T_0, v_0 is the characteristic molecular speed of the mixture defined as:

$$v_0 = \sqrt{\frac{2k_{\text{B}}T_0}{m}}, \quad m = C_0 m_1 + (1 - C_0)\, m_2, \tag{3}$$

m_α is the molecular mass of the species α.

Since the second species of the mixture can sublimate, its pressures are different at the two surfaces. Let p_{L2} and p_{U2} be pressures of the saturated vapor of Argon at the temperatures T_L and T_U, respectively. Thus, a temperature difference ΔT leads to some specific pressure difference $\Delta p_2 = p_{U2} - p_{L2}$. However, the pressure Δp_2 and temperature ΔT differences can be considered independent of each other when solving the problem. Let us introduce two independent thermodynamic forces related to the pressure and temperature differences as

$$X_{\text{P}} = \frac{\Delta p_2}{p_{02}}, \qquad X_{\text{T}} = \frac{\Delta T}{T_0}, \tag{4}$$

where $p_{02} = (1 - C_0)\, p_0$ is the partial equilibrium pressure of Argon. Since

$$|X_{\rm P}| \ll 1, \quad |X_{\rm T}| \ll 1, \tag{5}$$

the thermodynamic forces can be used as small parameters to linearize the kinetic equation.

Our aim is to calculate the mass $\dot{M}$ and energy $\dot{E}$ flow rates from the upper surface to lower one as function of the temperature T_0, the molar fraction C_0, the rarefaction parameter δ, and the differences Δp_2, ΔT. The problem is solved on the level of the velocity distribution functions $f_\alpha(y, \mathbf{v}_\alpha)$ of the two species, where $\mathbf{v}_\alpha$ is the molecular velocity vector of species α, see e.g. [26]. The flow rates of our interest are defined via the distribution functions as

$$\dot{M} = -\int m_2 v_{2y} f_2(y, \mathbf{v}_\alpha) {\rm d}\mathbf{v}_2, \tag{6}$$

$$\dot{E} = -\sum_{\alpha=1}^{2} \int \frac{1}{2} m_\alpha v_\alpha^2 v_{\alpha y} f_\alpha(y, \mathbf{v}_\alpha) {\rm d}\mathbf{v}_\alpha, \tag{7}$$

so that the quantities $\dot{M}$ and $\dot{E}$ are positive. Note that these quantities are independent of the coordinate y because of the mass and energy conservation laws.

3. Kinetic equation

The distribution functions $f_\alpha(y, \mathbf{v}_\alpha)$ needed to calculate the mass and energy flow rates are obtained from the Boltzmann type kinetic equation, which can be linearized using the assumption (5), i.e.

$$f_\alpha(y, \mathbf{v}_\alpha) = f_\alpha^M (1 + h_\alpha^{\rm P} X_{\rm P} + h_\alpha^{\rm T} X_{\rm T}), \qquad \alpha = 1, 2, \tag{8}$$

where h_α^P and h_α^T are the perturbation functions. The equilibrium distribution function, f_α^M, reads

$$f_\alpha^M = n_{0\alpha} \left(\frac{m_\alpha}{2\pi k_{\rm B} T_0} \right)^{3/2} \exp\left(-\frac{m_\alpha v_\alpha^2}{2 k_{\rm B} T_0} \right). \tag{9}$$

The perturbation functions of species α obey the two coupled linearized Boltzmann type kinetic equations per species [26]

$$\frac{\partial h_\alpha^{(i)}}{\partial t'} + v_{y\alpha}\frac{\partial h_\alpha^{(i)}}{\partial y'} = \sum_{\beta=1}^{2} \hat{Q}_{\alpha\beta} h_\beta^{(i)}\,, \quad i = P, T, \quad \alpha = 1, 2, \tag{10}$$

where $\hat{Q}_{\alpha\beta} h_\beta^{(i)}$ is the linearized collision operator between the species α and β. A numerical solution of the Boltzmann equation itself represents a hard computational task, see e.g. Refs. [27], [28], [29]. At the same time, the model kinetic equations provide reliable solution with modest computational effort [30, 31, 32].

Here, the McCormack model [33] is used to describe the collision term. To write down this model, it is convenient to introduce the following dimensionless quantities:

$$t = t'\frac{v_0}{H}, \qquad y = \frac{y'}{H}, \qquad \mathbf{c}_\alpha = \sqrt{\frac{m_\alpha}{2k_{\mathrm{B}}T_0}}\mathbf{v}_\alpha, \quad \alpha = 1, 2, \tag{11}$$

where $\mathbf{c}_\alpha$ is dimensionless molecular velocity of the species α. In terms of the above introduced dimensionless variables, the linearized Boltzmann type kinetic equations (10) become

$$\sqrt{\frac{m_\alpha}{m}}\frac{\partial h_\alpha^{(i)}}{\partial t} + c_{\alpha y}\frac{\partial h_\alpha^{(i)}}{\partial y} = \delta A \sqrt{\frac{m_\alpha}{m}} \sum_{\beta=1}^{2} \hat{L}_{\alpha\beta} h^{(i)}\,, \quad i = P, T, \quad \alpha = 1, 2, \tag{12}$$

where

$$A = \frac{C_0}{\gamma_1} + \frac{1 - C_0}{\gamma_2}. \tag{13}$$

In case of one-dimensional flow along the y-axis, the McCormack collisional term $\hat{L}_{\alpha\beta} h_\beta^{(i)}$ is provided in Appendix A, together with the $\upsilon_{\alpha\beta}^{(n)}$ functions. The dimensionless moments of the perturbation functions are given as

$$\nu_\alpha^{(i)} = \frac{1}{\pi^{3/2}} \int e^{-c_\alpha^2} h_\alpha^{(i)} \mathrm{d}\mathbf{c}_\alpha\,, \tag{14}$$

$$u_2^{(i)} = \frac{1}{\pi^{3/2}} \sqrt{\frac{m}{m_\alpha}} \int e^{-c_\alpha^2} h_2^{(i)} c_{2y} \mathrm{d}\mathbf{c}_2, \quad u_1^{(i)} = 0, \tag{15}$$

$$\tau_\alpha^{(i)} = \frac{1}{\pi^{3/2}} \int e^{-c_\alpha^2} h_\alpha^{(i)} \left(\frac{2}{3} c_\alpha^2 - 1 \right) \mathrm{d}\mathbf{c}_\alpha \,, \tag{16}$$

$$\Pi_\alpha^{(i)} = \frac{1}{\pi^{3/2}} \int e^{-c_\alpha^2} h_\alpha^{(i)} \left(c_{\alpha y}^2 - \frac{1}{3} c_\alpha^2 \right) \mathrm{d}\mathbf{c}_\alpha \,, \tag{17}$$

$$q_\alpha^{(i)} = \frac{1}{\pi^{3/2}} \sqrt{\frac{m}{m_\alpha}} \int e^{-c_\alpha^2} h_\alpha^{(i)} c_{\alpha y} \left(c_\alpha^2 - \frac{5}{2} \right) \mathrm{d}\mathbf{c}_\alpha \,. \tag{18}$$

The parameters $\gamma_{\alpha\beta}$ are proportional to the collision frequency between species α and β and appear in the collision term (A.1) only in the combinations $\gamma_1 = \gamma_{11} + \gamma_{12}$ and $\gamma_2 = \gamma_{21} + \gamma_{22}$, so we need to define only γ_1 and γ_2. The collision frequencies γ_α can be written in the same manner as in the Shakhov kinetic model [34, 35, 36]:

$$\gamma_\alpha = \frac{p_{0\alpha}}{\mu_\alpha}, \tag{19}$$

where $p_{0\alpha} = n_{0\alpha} k_\mathrm{B} T_0$ is the equilibrium partial pressure and μ_α is the partial viscosity given as

$$\mu_\alpha = p_{0\alpha} \frac{S_\beta + \upsilon_{\alpha\beta}^{(4)}}{S_\alpha S_\beta - \upsilon_{\alpha\beta}^{(4)} \upsilon_{\beta\alpha}^{(4)}}, \quad S_\alpha = \upsilon_{\alpha\alpha}^{(3)} - \upsilon_{\alpha\alpha}^{(4)} + \upsilon_{\alpha\beta}^{(3)}, \quad \text{and} \quad \beta \neq \alpha. \tag{20}$$

Other details on the dimensionless presentation of omega integrals (A.6) and $\upsilon_{\alpha\beta}^{(i)}$ functions (A.2), as well as S_α can be found in [32, 37].

Once the dimensionless moments (14)-(18) are known from the solution of Eqs. (12), the number density and temperature of species α are calculated as

$$n_\alpha = n_{0\alpha} \left(1 + \nu_\alpha^P X_P + \nu_\alpha^T X_T \right), \tag{21}$$

$$T_\alpha = T_0 \left(1 + \tau_\alpha^P X_P + \tau_\alpha^T X_T \right). \tag{22}$$

The corresponding quantities of the binary mixture are defined as

$$n = n_1 + n_2, \tag{23}$$

$$T = C_0 T_1 + (1 - C_0) T_2. \tag{24}$$

The mass $\dot{M}$ and energy $\dot{E}$ flow rates can be expressed in terms of the kinetic coefficients Λ_{ij} defined via the dimensionless moments as

$$\Lambda_{\mathrm{Pi}} = -(1 - C_0) u_2^{(i)}, \quad \Lambda_{\mathrm{Ti}} = -C_0 q_1^{(i)} - (1 - C_0) q_2^{(i)}, \quad i = P, T. \tag{25}$$

Following the formalism of irreversible thermodynamics [38], the thermodynamic fluxes are represented as

$$J_{\mathrm{P}} = \Lambda_{\mathrm{PP}} X_{\mathrm{P}} + \Lambda_{\mathrm{PT}} X_{\mathrm{T}}, \tag{26}$$

$$J_{\mathrm{T}} = \Lambda_{\mathrm{TP}} X_{\mathrm{P}} + \Lambda_{\mathrm{TT}} X_{\mathrm{T}}. \tag{27}$$

Then, the mass $\dot{M}$ and energy $\dot{E}$ flow rates defined by (6) and (7) are obtained in terms of the thermodynamics fluxes as

$$\dot{M} = n_0 m_2 v_0 J_{\mathrm{P}}, \quad \dot{E} = p_0 v_0 \left(J_{\mathrm{T}} + \frac{5}{2} J_{\mathrm{P}} \right). \tag{28}$$

As it was shown in Ref. [38], the matrix Λ_{ij} is symmetric, *i.e.*, $\Lambda_{\mathrm{PT}} = \Lambda_{\mathrm{TP}}$, so that the mass and energy transfer is determined by the three independent coefficients. Moreover, the entropy production σ (never negative) in the system per area unit of the surfaces is expressed in terms of the kinetic coefficients as

$$\sigma = \frac{n_0 v_0}{T_0} \sum_{i,j=1}^{2} \Lambda_{ij} X_i X_j > 0. \tag{29}$$

The matrix Λ_{ij} must be positive definite in order to keep the entropy production positive.

4. Boundary conditions

According to the problem statement, the first species is diffusely scattered from each solid surface so that the boundary conditions at $y = 1/2$ and $c_{1y} < 0$

read

$$h_1^P = \nu_{1w}^P, \quad h_1^T = \frac{1}{2}\left(c_1^2 - \frac{5}{2}\right) + \nu_{1w}^T, \tag{30}$$

where ν_{1w}^P and ν_{1w}^T are calculated from the impermeability condition

$$\nu_{1\mathrm{w}}^{(i)} = \frac{2}{\pi}\int_{c_{1y}>0} h_1^{(i)} c_{1y} e^{-c_1^2} \mathrm{d}\mathbf{c}_1, \quad i = P, T. \tag{31}$$

The perturbation function of particles reflected from the lower surface is given by the symmetry condition

$$h_\alpha^{(i)}(y, c_{1y}) = -h_\alpha^{(i)}(-y, -c_{1y}). \tag{32}$$

The particles of the second species are not reflected, but they are completely absorbed by the surfaces. At the same time, the surfaces emit particles of this species with the Maxwellian distribution function. For instance, the Maxwellian of the upper surface reads

$$f_{2\mathrm{U}}^{\mathrm{M}} = n_{\mathrm{U}}\left(\frac{m_2}{2\pi k_{\mathrm{B}} T_{\mathrm{U}}}\right)^{3/2} \exp\left(-\frac{m_2 v_2^2}{2k_{\mathrm{B}} T_{\mathrm{U}}}\right), \tag{33}$$

where n_{U} is the density of saturated vapor at the temperature T_{U}. Thus, the perturbation function of the emitted particle at $y = 1/2$ and $c_{2y} < 0$ is given as

$$h_2^{\mathrm{P}} = \frac{1}{2}, \quad h_2^{\mathrm{T}} = \frac{1}{2}\left(c_2^2 - \frac{5}{2}\right). \tag{34}$$

The perturbation function at $y = -1/2$ and $c_{2y} > 0$ has just the opposite sign according to (32).

5. Method of solution

The Discrete Velocity Method (DVM) is used to solve the McCormack kinetic equations (12). To reduce computational efforts, the $c_{\alpha z}$ variable is eliminated

by introducing the reduced functions of $h_\alpha^{(i)}$:

$$\begin{aligned}\Phi_\alpha^{(i)} &= \frac{1}{\sqrt{\pi}}\sqrt{\frac{m}{m_\alpha}}\int h_\alpha^{(i)}\exp\left(-c_{\alpha z}^2\right)dc_{\alpha z},\\ \Psi_\alpha^{(i)} &= \frac{1}{\sqrt{\pi}}\sqrt{\frac{m}{m_\alpha}}\int h_\alpha^{(i)}c_{\alpha z}^2\exp\left(-c_{\alpha z}^2\right)dc_{\alpha z},\end{aligned} \tag{35}$$

$\alpha = 1, 2$ and $i = P, T$.

The DVM consists of splitting the continuum molecular velocity space c_x, c_y in Eq. (12) into discrete velocity sets c_{x_m}, c_{y_k}, where $m, k = \pm 1, ... \pm N_c$. These velocities c_{x_m}, c_{y_k}, are taken to be the roots of the Hermit polynomial of order N_c. Then the set of $2N_c$ kinetic equations, corresponding to $2N_c$ values of discrete velocities, is discretized in time and space by finite difference method (FDM). Here N_c is taken to be equal to 20. The grid-independence in molecular velocity space is checked by using a finer grid of 50×50 points ($N_c = 25$) resulting the variation of all macroscopic quantities within 1%. The spacial derivatives are approximated by the second-order accurate Total Variation Diminishing (TVD) type scheme as in Ref. [39]. The number of uniformly distributed points in physical space N_y is equal to 1000, which insures the numerical error of 1% of the simulations.

The time derivative is approximated by the time-explicit Euler method. The time step $\Delta t = 0.42$, chosen according to the condition by Courant-Friedrichs-Lewy [40], provides the numerical error less than 1%. The stationary solution was considered for our purpose with a relative convergence criterion equal to 10^{-7} for all moments of the perturbation functions.

To check the numerical code, some particular situations corresponding to previously published results have been resolved. In case $C_0 = 1$, the problem is reduced to the heat transfer through a single non-condensable gas reported previously in Ref. [41]. If we assume $C_0 = 0$, then the single gas sublimation and deposition processes are simulated. The analogous formulation was considered

	T=50 K	T=70 K
$\mu_1 \times 10^6$ [Pa·s][45]	6.0842	7.5682
$\mu_2 \times 10^6$ [Pa·s][24]	4.31945	5.79674
d_2/d_1	2.109	2.031

Table 1: Viscosities of Helium, μ_1, and Argon, μ_2, and the ratio of their molecular diameters, d_2/d_1, for the reference temperatures.

in Refs. [42, 43] in the case of evaporation and condensation. Finally, if we assume that the second species is also non-condensable, then the problem will be the same as that considered in Ref. [44]. Applying the elaborated numerical codes to these particular situations, we can reproduced the results reported in Refs. [41, 42, 43, 44] within the numerical error.

The specific temperature range was chosen, where Helium can not be in a solid state while Argon can sublimate and deposit. Two values of the reference temperature, $T_0 = 50$ K and 70 K, are chosen based on the sublimation curve of Argon provided in [23]. The following values of molecular masses are used in numerical simulations: $m_1 = 6.6465 \times 10^{-27}$ kg and $m_2 = 66.335 \times 10^{-27}$ kg. The gas viscosities of Helium and Argon calculated *ab initio* in [45, 24] are provided in Table 1 for two reference temperatures.

6. Intermolecular potentials

The model collision integral (A.1) contains the quantities $\nu_{\alpha\beta}^{(n)}$ expressed in terms of the Ω integrals by Eq. (A.2). In turn, these integrals are determined by the intermolecular potential via the differential cross section so that the solution of the problem considered here is influenced by the potential. To quantify this influence three types of the potential are used in the simulations: the Hard Sphere (HS), Lennard-Jones (LJ), and *ab initio* (AI) [46]. The HS potential is the most simple potential because it contains only one fitting parameter, namely, the molecular diameter d_i. Dimensionless numerical results for a single gas based

on this potential are independent of the gas species and its temperature. That is why the HS potential is widely used in rarefied gas dynamics simulations. In case of binary gaseous mixture, the Ω integrals are calculated analytically using Eq.(A.6). Since the right-hand-side of Eq. (12) contains only the Ω integral ratios, to solve it we need to specify only the mass ratio and diameter ratio, d_2/d_1. The last one can be expressed via the viscosities of single gases as

$$\frac{d_2}{d_1} = \left(\frac{\mu_1}{\mu_2}\right)^{1/2} \left(\frac{m_2}{m_1}\right)^{1/4}. \tag{36}$$

The ratio follows from the analytical expression of viscosity for hard sphere gas [25]. The values of d_2/d_1 based on the *ab initio* viscosities are presented in Table 1 for two reference temperatures.

The LJ potential given as

$$V(r) = 4\varepsilon \left[\left(\frac{d}{r}\right)^{12} - \left(\frac{d}{r}\right)^{6}\right] \tag{37}$$

contains two fitting parameters: well-depth ε and zero-point d. In contrast to HS, this potential takes into consideration the attractive force and provides more physical results. In this case, the Ω integrals (A.4) are calculated numerically for each species and for some specific temperature. However, if the reduced temperature $T^* = k_{\text{B}}T/\varepsilon$ is introduced, the Ω integrals are tabulated in terms of T^* and then they can be used for any gaseous species and their mixtures. Thus, the use of T^* reduces computational cost to solve the kinetic equation.

The AI potentials obtained numerically from the Schrödinger equation are free from any adjustable parameter. To make easier the use of these potentials, their numerical values are presented analytically using a set of interpolating coefficients. For our purpose, we used the potentials reported in Refs. [47, 48] and [49] for the collisions He-He, Ar-Ar, and He-Ar, respectively. The well-depths and zero-points of these potentials are given in Table 2. A comparison

	d (nm)	ϵ/k (K)	Ref.
He-He	0.26410	10.996	[47]
Ar-Ar	0.33577	142.94	[48]
He-Ar	0.31169	29.760	[49]

Table 2: Well-depth and zero-point of AI potentials.

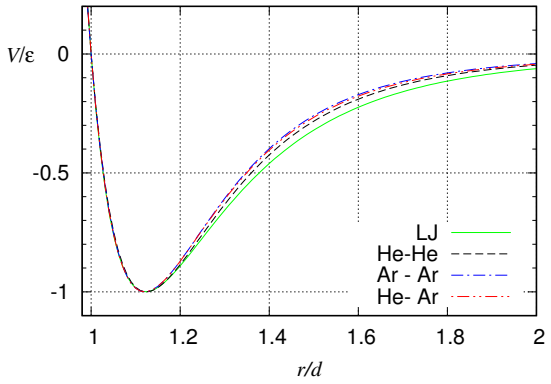

Figure 1: Comparison of *ab initio* potentials with the Lennard-Jones one.

of AI potentials with the LJ one is performed in Figure 1, which shows that the AI potentials are close to the LJ one near the well, but their asymptotic behaviors at $r \to \infty$ are different. Such a difference can cause an influence of the potential on macroscopic characteristics at some temperatures.

To implement LJ and AI potentials, the Ω integrals have been calculated numerically by the method described in details in Ref. [24]. In case of the LJ, the well depths and zero-points given in Table 2 have been substituted into the expression (37). The interpolating expressions given in Refs. [47, 48, 49] have been used for the AI potentials. The numerical values of the Ω integrals for both LJ and AI potentials are provided in Table 3, which shows that the discrepancy between the two potentials is about 2% for most of the integrals and it reaches 9% for $\Omega_{22}^{(22)}$.

$\Omega_{\alpha\beta}^{(nm)} \times 10^{16}$ $[m^3/\mathrm{s}]$	LJ		AI	
	T_0=50 K	70 K	T_0=50 K	70 K
$\Omega_{12}^{(11)}$	0.460412	0.487594	0.452601	0.479487
$\Omega_{12}^{(12)}$	1.211720	1.319461	1.193073	1.296515
$\Omega_{12}^{(13)}$	4.514291	4.983730	4.440914	4.885739
$\Omega_{11}^{(22)}$	0.730863	0.824615	0.714749	0.804336
$\Omega_{22}^{(22)}$	1.094076	1.114277	1.000645	1.042668
$\Omega_{12}^{(22)}$	1.000723	1.062131	0.988153	1.051521

Table 3: Values of Ω-integrals based on LJ and AI potential vs temperature T.

7. Results and discussions

Figures 2 - 4 present the profiles of dimensionless quantities, $\nu_\alpha^{(i)}$ and $\tau_\alpha^{(i)}$, for both species, obtained with HS (solid line) and AI (dashed line) potentials for the mole fraction equal to 0.1, 0.5 and 0.9, respectively. For each value of mole fraction three values of the rarefaction parameter are provided, $\delta = 0.1$, 1 and 10. Note, all profiles are symmetric relatively the middle point of the gap that is a consequence of the linearization of the kinetic equation. The dependence of the density deviation of Helium is linear in the most of cases, while the density deviation of Argon represents a non-linear behavior with respect to the y coordinate near the solid surface. The density deviations of both Helium and Argon are slightly sensitive to the intermolecular potential.

Considering the temperature deviation curves, $\tau_\alpha^{(i)}$, a very pronounced non-linear behavior is observed for Helium, τ_1^P curve, for all values of the mole fraction. The temperature deviation of Argon becomes also slightly non-linear for $C_0 = 0.9$, *i.e.* for low Argon mole fraction. For all these temperature deviation curves, only for temperature variations due to the pressure gradient, τ_1^P curve for Helium, the difference between the two potentials is significant. For all other cases both potentials provide very similar results.

The matrix of the kinetic coefficients Λ_{ij}, calculated with HS, AI, and LJ

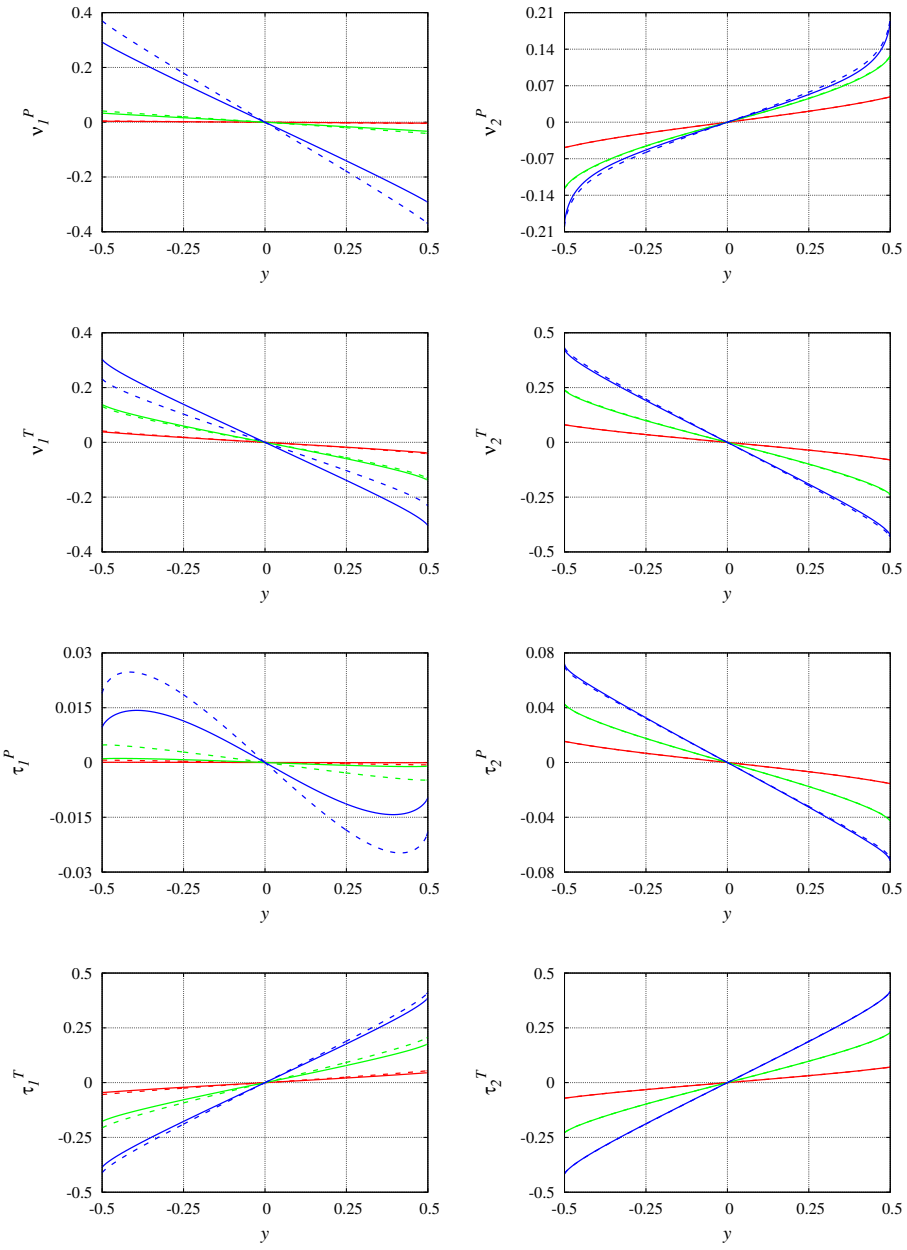

Figure 2: Deviations of density, ν_α^i, and temperature, τ_α^i, $\alpha = 1, 2$, $i = P, T$, defined by Eqs. (14), (16), vs the coordinate y at $C_0 = 0.1$ and $T_0 = 50$ K: red lines - $\delta = 0.1$, green lines - $\delta = 1$, blue lines $\delta = 10$; solid lines - HS, dashed lines - AI potential.

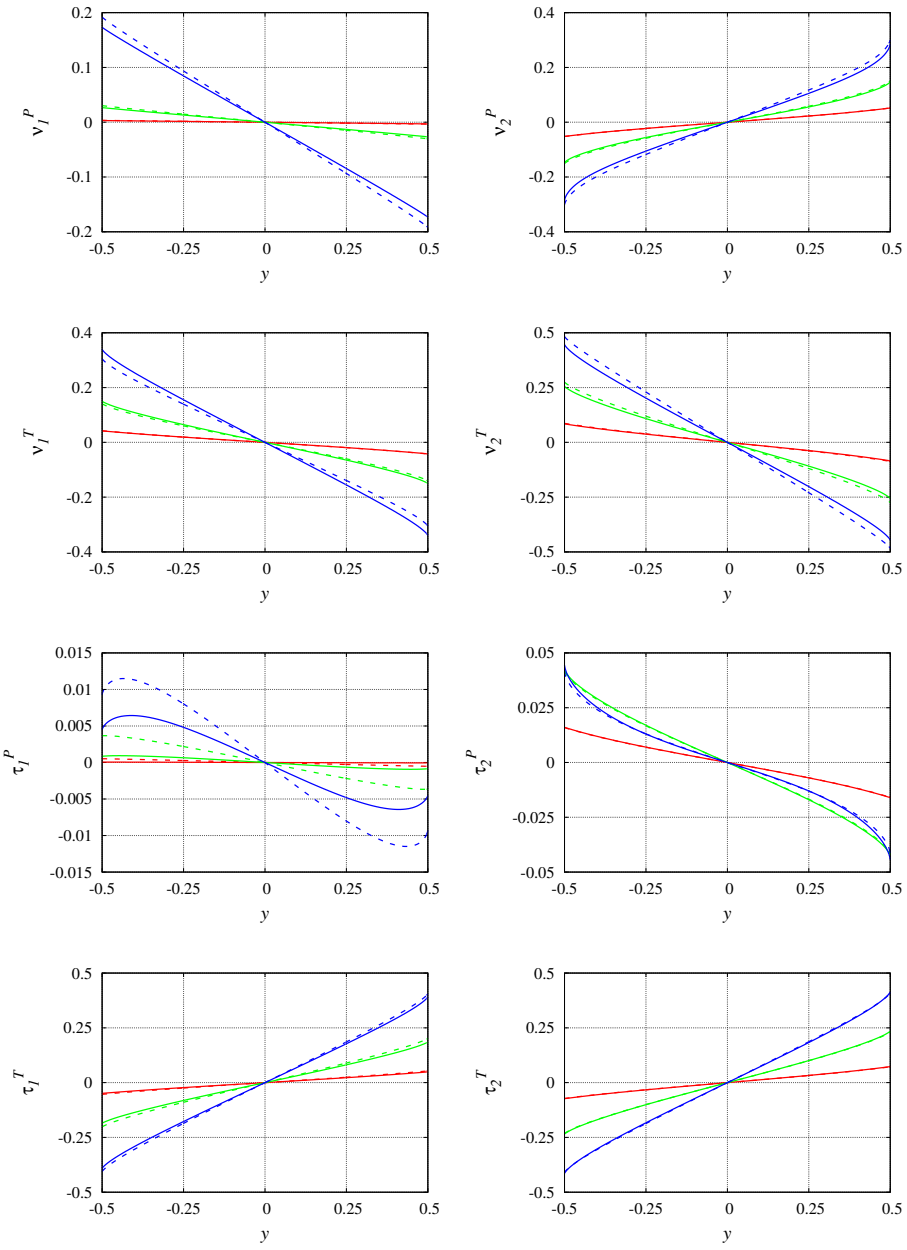

Figure 3: Deviations of density, ν_α^i, and temperature, τ_α^i, $\alpha = 1, 2$, $i = P, T$, defined by Eqs. (14), (16), vs the coordinate y at $C_0 = 0.5$ and $T_0 = 50$ K: red lines - $\delta = 0.1$, green lines - $\delta = 1$, blue lines $\delta = 10$; solid lines - HS, dashed lines - AI potential.

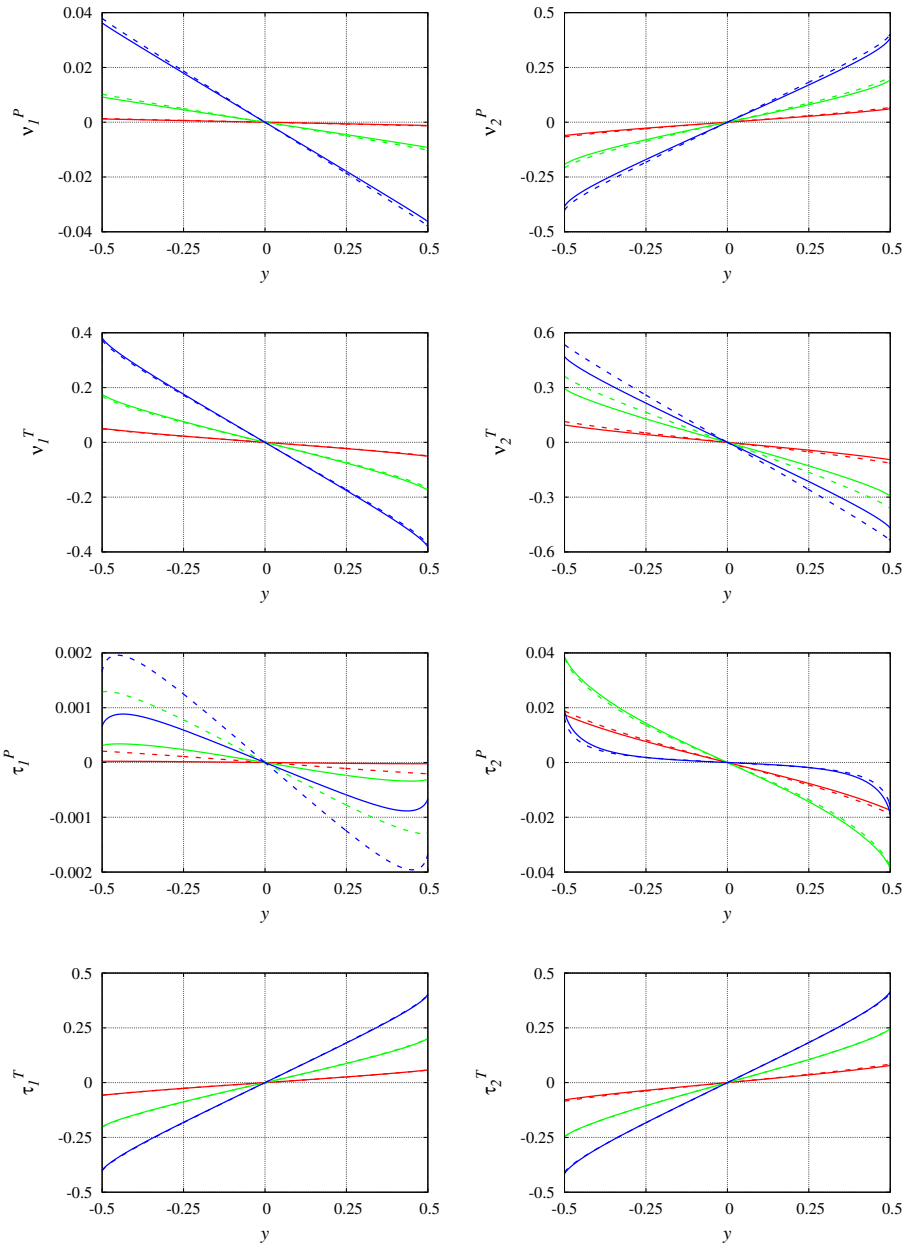

Figure 4: Deviations of density, ν_α^i, and temperature, τ_α^i, $\alpha = 1, 2$, $i = P, T$, defined by Eqs. (14), (16), vs the coordinate y at $C_0 = 0.9$ and $T_0 = 50$ K: red lines - $\delta = 0.1$, green lines - $\delta = 1$, blue lines $\delta = 10$; solid lines - HS, dashed lines - AI potential.

potentials for equilibrium temperature $T_0 = 50$ K and for three equilibrium mole fractions $C_0 = 0.1$, 0.5, and 0.9, are provided in Tables 4 - 6, respectively. It has been verified that the Onsager reciprocity relations, $\Lambda_{\rm PT} = \Lambda_{\rm TP}$, are fulfilled within the numerical accuracy so that the two coefficients are presented in one column of Tables 4 - 6. Note that the diagonal kinetic coefficients $\Lambda_{\rm PP}$ and $\Lambda_{\rm TT}$ are always positive, while the cross kinetic coefficients, $\Lambda_{\rm PT}$ and $\Lambda_{\rm TP}$, can be negative and positive. The values of the cross coefficients are quite smaller than those of the diagonal coefficients that guarantees the matrix Λ_{ij} to be positive definite. The results obtained with AI and LJ potentials are very close to each other for all considered rarefaction parameters and mole fraction ranges. However, the difference of the results based on the AI and HS potentials is quite larger. Analyzing the numerical data on the kinetic coefficients we can observe that the maximum discrepancy between the coefficient $\Lambda_{\rm PP}$ obtained for the AI and HS potentials reaches 17% at $C_0 = 0.9$ and $\delta = 10$. This difference decreases by decreasing the mole fraction C_0. The same analysis for the coefficient $\Lambda_{\rm TT}$ shows that the maximum discrepancy because of the potential is about 13% and it takes place at $C_0 = 0.5$ and $\delta = 20$. As expected, the cross coefficients, $\Lambda_{\rm PT}$ and $\Lambda_{\rm TP}$, are much sensitive to the intermolecular potential. The maximal difference in the cross-coefficients, $\Lambda_{\rm PT}$, reaches 100% for the same set of parameters, $C_0 = 0.5$ and $\delta = 20$. In some cases, see e.g. $C_0 = 0.5$ and $\delta = 20$, the cross coefficients obtained for the AI and HS potentials, have the opposite sign. For all kinetic coefficients, the difference in their values obtained from two potentials decreases with decreasing of the rarefaction parameter.

To study the temperature influence on the kinetic coefficients, similar calculations have been carried out for equilibrium temperature $T_0 = 70$ K. The

δ	Hard Sphere			*ab-initio* potential			Lennard-Jones potential		
	Λ_{PP}	$\Lambda_{PT} = \Lambda_{TP}$	Λ_{TT}	Λ_{PP}	$\Lambda_{PT} = \Lambda_{TP}$	Λ_{TT}	Λ_{PP}	$\Lambda_{PT} = \Lambda_{TP}$	Λ_{TT}
0.1	0.2367	-0.1113	0.6737	0.2367	-0.1115	0.6758	0.2367	-0.1115	0.6760
1	0.2188	-0.0750	0.4891	0.2193	-0.0767	0.5002	0.2194	-0.0767	0.5015
2	0.2112	-0.0572	0.3887	0.2123	-0.0598	0.4031	0.2125	-0.0599	0.4049
5	0.2001	-0.0325	0.2469	0.2024	-0.0366	0.2624	0.2028	-0.0367	0.2645
10	0.1889	-0.0168	0.1930	0.1930	-0.0216	0.1681	0.1938	-0.0217	0.1700
20	0.1728	-0.0059	0.0893	0.1796	-0.0109	0.0982	0.1810	-0.0110	0.0996

Table 4: Kinetic coefficients for HS, AI and LJ potentials vs rarefaction parameter δ at $C_0 = 0.1$ and $T_0 = 50$K.

δ	Hard Sphere			*ab-initio* potential			Lennard-Jones potential		
	Λ_{PP}	$\Lambda_{PT} = \Lambda_{TP}$	Λ_{TT}	Λ_{PP}	$\Lambda_{PT} = \Lambda_{TP}$	Λ_{TT}	Λ_{PP}	$\Lambda_{PT} = \Lambda_{TP}$	Λ_{TT}
0.1	0.1015	-0.0468	0.8506	0.1016	-0.0475	0.8555	0.1016	-0.0475	0.8561
1	0.0887	-0.0245	0.6286	0.0899	-0.0294	0.6551	0.0900	-0.0294	0.6582
2	0.0812	-0.0135	0.5031	0.0833	-0.0208	0.5374	0.0836	-0.0209	0.5414
5	0.0675	-0.0000	0.3242	0.0710	-0.0096	0.3599	0.0715	-0.0098	0.3644
10	0.0536	0.0060	0.2071	0.0580	-0.0034	0.2358	0.0588	-0.0035	0.2397
20	0.0383	0.0075	0.1214	0.0427	-0.0000	0.1403	0.0435	-0.0002	0.1431

Table 5: Kinetic coefficients for HS, AI and LJ potentials vs rarefaction parameter δ at $C_0 = 0.5$ and $T_0 = 50$K.

δ	Hard Sphere			*ab-initio* potential			Lennard-Jones potential		
	Λ_{PP}	$\Lambda_{PT} = \Lambda_{TP}$	Λ_{TT}	Λ_{PP}	$\Lambda_{PT} = \Lambda_{TP}$	Λ_{TT}	Λ_{PP}	$\Lambda_{PT} = \Lambda_{TP}$	Λ_{TT}
0.1	0.0116	-0.0050	0.6920	0.0117	-0.0054	0.6926	0.0117	-0.0054	0.6930
1	0.0088	-0.0006	0.5218	0.0092	-0.0025	0.5267	0.0092	-0.0025	0.5270
2	0.0071	0.0011	0.4240	0.0077	-0.0013	0.4300	0.0077	-0.0014	0.4303
5	0.0047	0.0023	0.2795	0.0054	-0.0012	0.2851	0.0054	-0.0002	0.2855
10	0.0030	0.0022	0.1807	0.0036	0.0003	0.1847	0.0016	0.0002	0.1850
20	0.0018	0.0016	0.1063	0.0021	0.0003	0.1087	0.0022	0.0003	0.1089

Table 6: Kinetic coefficients for HS, AI and LJ potentials vs rarefaction parameter δ at $C_0 = 0.9$ and $T_0 = 50$K.

corresponding coefficients, obtained for the three potentials, are provided in Table 7 - 9, for $C_0 = 0.1$, 0.5 and 0.9, respectively. These data show that the diagonal coefficients are weakly sensitive to the temperature, while the cross coefficients are strongly sensitive to the temperature T_0 for large values of the gas rarefaction.

One of the important characteristics of the sublimation-deposition process is

δ	Hard Sphere			*ab-initio* potential			Lennard-Jones potential		
	Λ_{PP}	$\Lambda_{PT} = \Lambda_{TP}$	Λ_{TT}	Λ_{PP}	$\Lambda_{PT} = \Lambda_{TP}$	Λ_{TT}	Λ_{PP}	$\Lambda_{PT} = \Lambda_{TP}$	Λ_{TT}
0.1	0.2367	-0.1113	0.6737	0.2367	-0.1115	0.6756	0.2367	-0.1115	0.6758
1	0.2188	-0.0749	0.4884	0.2193	-0.0765	0.4994	0.2194	-0.0765	0.5003
2	0.2112	-0.0572	0.3878	0.2123	-0.0595	0.4021	0.2124	-0.0595	0.4033
5	0.1999	-0.0325	0.2461	0.2023	-0.0360	0.2612	0.2026	-0.0360	0.2625
10	0.1886	-0.0167	0.1545	0.1929	-0.0208	0.1671	0.1934	-0.0209	0.1682
20	0.1721	-0.0059	0.0889	0.1793	-0.0100	0.0975	0.1803	-0.0101	0.0983

Table 7: Kinetic coefficients for HS, AI and LJ potentials vs rarefaction parameter δ at $C_0 = 0.1$ and $T_0 = 70$K.

δ	Hard Sphere			*ab-initio* potential			Lennard-Jones potential		
	Λ_{PP}	$\Lambda_{PT} = \Lambda_{TP}$	Λ_{TT}	Λ_{PP}	$\Lambda_{PT} = \Lambda_{TP}$	Λ_{TT}	Λ_{PP}	$\Lambda_{PT} = \Lambda_{TP}$	Λ_{TT}
0.1	0.1015	-0.0468	0.8502	0.1016	-0.0474	0.8550	0.1016	-0.0474	0.8554
1	0.0887	-0.0245	0.6268	0.0899	-0.0288	0.6525	0.0900	-0.0288	0.6544
2	0.0812	-0.0135	0.5009	0.0833	-0.0198	0.5340	0.0835	-0.0198	0.5363
5	0.0673	-0.0000	0.3219	0.0710	-0.0082	0.3562	0.0714	-0.0082	0.3588
10	0.0534	0.0060	0.2053	0.0580	-0.0018	0.2327	0.0586	-0.0018	0.2349
20	0.0381	0.0074	0.1201	0.0428	0.0014	0.1382	0.0433	0.0014	0.1398

Table 8: Kinetic coefficients for HS, AI and LJ potentials vs rarefaction parameter δ at $C_0 = 0.5$ and $T_0 = 70$K.

δ	Hard Sphere			*ab-initio* potential			Lennard-Jones potential		
	Λ_{PP}	$\Lambda_{PT} = \Lambda_{TP}$	Λ_{TT}	Λ_{PP}	$\Lambda_{PT} = \Lambda_{TP}$	Λ_{TT}	Λ_{PP}	$\Lambda_{PT} = \Lambda_{TP}$	Λ_{TT}
0.1	0.0116	-0.0050	0.6919	0.0118	-0.0054	0.6926	0.0118	-0.0054	0.6927
1	0.0088	-0.0007	0.5214	0.0093	-0.0023	0.5255	0.0093	-0.0023	0.5255
2	0.0072	0.0010	0.4234	0.0078	-0.0011	0.4285	0.0078	-0.0011	0.4285
5	0.0048	0.0023	0.2790	0.0055	0.0002	0.2836	0.0055	0.0002	0.2835
10	0.0031	0.0022	0.1802	0.0037	0.0006	0.1835	0.0037	0.0006	0.1835
20	0.0018	0.0011	0.1063	0.0022	0.0005	0.1079	0.0022	0.0006	0.1079

Table 9: Kinetic coefficients for HS, AI and LJ potentials vs rarefaction parameter δ at $C_0 = 0.9$ and $T_0 = 70$K.

the sublimation-deposition rate (26) and the heat flux (27) through the gas-solid interface. To compare the results of the sublimation rate between the potentials considered here for two reference temperatures, $T_0 = 50$ K and 70 K, the corresponding saturation pressures, p_s, are calculated using Eq. (B.1) proposed in Ref. [23]. This equation shows that a very small change in the temperature generates a large variation of the saturated vapor pressure. Therefore here, a

very small difference of the temperature is considered, namely $\Delta T/T_0 = 0.004$, which leads to a relatively large pressure difference, i.e., $\Delta p_2/p_{02} = 0.083$ and 0.068 for the temperature T_0 equal to 50 K and 70 K, respectively. These values of the pressure differences are still reasonable and the linearized approach can be applied. The sublimation flow rate (26) and the heat transfer through interface (27) for different mole fractions, for different values of the rarefaction parameter and for the driving forces equal to $X_P = 0.083$ and $X_T = 0.004$, are provided in Tables 10 and 11 for three potentials, HS, LJ, and AI. The results for the temperature 70 K and $X_P = 0.068$ and $X_T = 0.004$ are provided in Tables 12 and 13, also for both potentials.

As it can be observed from Table 10 the sublimation flux $J_{\rm P}$ is directed from the hotter surface, $y = 0.5$, to the colder one, $y = -0.5$. The absolute value of the sublimation flow rate decreases by increasing the rarefaction parameter. In addition, this flow rate decreases also with the increasing of the Helium mole fraction, which is the natural trend because Helium does not sublimate or deposit in the considered temperature range. The values of the sublimation flow rate, obtained for the two potentials, are slightly different. Generally, the values of sublimation flow rate, obtained with AI potential are larger than that calculated with HS one, with the maximal difference of 15% at $C_0 = 0.9$ and $\delta = 20$. This tendency is conserved with the reference temperature increasing up to 70K, see Table 12.

One can see from Table 11 that the heat flux $J_{\rm T}$ has the direction opposite to the sublimation rate, *i.e.* the heat flows from the colder surface, $y = -0.5$, the hotter one, $y = 0.5$, in case of the small mole fraction of Helium $C_0 = 0.1$. When the mole fraction increases up to $C_0 = 0.5$, the heat flux changes the sign from the rarefaction parameter equal to 1. It is worth to note that the direction

of the heat flux does not contradict to any thermodynamic law because the total energy flux given by Eq.(28) is directed from the hotter surface to the colder one. In general, the absolute value of the heat flux decreases when the rarefaction parameter increases and it has the maximal values for $C_0 = 0.5$. The difference between the heat flux values obtained from AI and HS potentials is much larger compared to that for the sublimation flow rate, with the maximal difference of 86% for $C_0 = 0.1$ and $\delta = 20$. The difference of both $J_{\rm P}$ and $J_{\rm T}$ obtained for the AI and LJ potentials is very small. In most of case, this difference does not exceed the numerical error.

	$J_{\rm P} \times 10^2$ (HS)			$J_{\rm P} \times 10^2$ (AI)			$J_{\rm P} \times 10^2$ (LJ)		
δ	$C_0 = 0.1$	0.5	0.9	0.1	0.5	0.9	0.1	0.5	0.9
0.1	2.108	1.495	0.497	2.108	1.497	0.500	2.108	1.497	0.500
1	1.961	1.319	0.380	1.965	1.334	0.396	1.966	1.336	0.397
2	1.810	1.215	0.314	1.908	1.241	0.334	1.910	1.245	0.335
5	1.809	1.017	0.210	1.828	1.063	0.233	1.832	1.071	0.234
10	1.714	0.812	0.136	1.749	0.872	0.156	1.757	0.883	0.157
20	1.571	0.582	0.080	1.631	0.644	0.094	1.644	0.657	0.095

Table 10: Sublimation flow rate $J_{\rm P}$ defined by (26) vs. mole fraction C_0 and rarefaction parameter δ at $T_0 = 50$ K assuming $X_{\rm T} = 0.004$ and $X_{\rm P} = 0.083$.

	$J_{\rm T} \times 10^3$ (HS)			$J_{\rm T} \times 10^3$ (AI)			$J_{\rm T} \times 10^3$ (LJ)		
δ	$C_0 = 0.1$	0.5	0.9	0.1	0.5	0.9	0.1	0.5	0.9
0.1	-6.54	-0.48	2.35	-6.55	-0.52	2.33	-6.55	-0.52	2.33
1	-4.27	0.48	2.04	-4.36	0.18	1.90	-4.36	0.19	1.90
2	-3.20	0.89	1.79	-3.35	0.43	1.61	-3.35	0.43	1.61
5	-1.71	1.29	1.31	-1.99	0.64	1.13	-1.99	0.65	1.13
10	-0.77	1.33	0.91	-1.12	0.66	0.76	-1.12	0.67	0.76
20	-0.13	1.11	0.56	-0.51	0.56	0.46	-0.52	0.56	0.46

Table 11: Heat flux $J_{\rm T}$ defined by (27) vs. mole fraction C_0 and rarefaction parameter δ at $T_0 = 50$ K assuming $X_{\rm T} = 0.004$ and $X_{\rm P} = 0.083$.

Figures 5 - 7 present the profiles of the macroscopic parameters of the mixture, namely of the temperature T calculated by Eq. (24), pressure $p = nk_{\rm B}T$ with density given by Eq. (23), and local mole fraction $C = n_1/(n_1 + n_2)$ with

	$J_{\rm P} \times 10^2$ (HS)			$J_{\rm P} \times 10^2$ (*ab-initio*)			$J_{\rm P} \times 10^2$ (Lennard-Jones)		
δ	$C_0 = 0.1$	0.5	0.9	0.1	0.5	0.9	0.1	0.5	0.9
0.1	1.718	1.219	0.406	1.718	1.220	0.409	1.718	1.220	0.409
1	1.600	1.077	0.313	1.604	1.090	0.327	1.604	1.091	0.327
2	1.551	0.993	0.260	1.558	1.015	0.277	1.559	1.017	0.278
5	1.478	0.831	0.176	1.494	0.871	0.195	1.497	0.875	0.196
10	1.400	0.664	0.115	1.431	0.715	0.132	1.435	0.722	0.133
20	1.282	0.478	0.068	1.334	0.529	0.080	1.341	0.536	0.080

Table 12: Sublimation flow rate $J_{\rm P}$ defined by (26) vs. mole fraction C_0 and rarefaction parameter δ at $T_0 = 70$ K assuming $X_{\rm T} = 0.004$ and $X_{\rm P} = 0.068$.

	$J_{\rm T} \times 10^3$ (HS)			$J_{\rm T} \times 10^3$ (*ab-initio*)			$J_{\rm T} \times 10^3$ (Lennard-Jones)		
δ	$C_0 = 0.1$	0.5	0.9	0.1	0.5	0.9	0.1	0.5	0.9
0.1	-4.87	0.22	2.43	-4.88	0.19	2.41	-4.88	0.20	2.41
1	-3.14	0.84	2.04	-3.20	0.65	1.94	-3.20	0.66	1.94
2	-2.33	1.08	1.76	-2.44	0.79	1.64	-2.43	0.80	1.64
5	-1.22	1.28	1.27	-1.40	0.87	1.15	-1.40	0.88	1.15
10	-0.52	1.23	0.87	-0.75	0.81	0.77	-0.75	0.82	0.77
20	-0.04	0.98	0.53	-0.29	0.65	0.47	-0.29	0.65	0.47

Table 13: Heat flux $J_{\rm T}$ defined by (27) vs. mole fraction C_0 and rarefaction parameter δ at $T_0 = 70$ K assuming $X_{\rm T} = 0.004$ and $X_{\rm P} = 0.068$.

the number densities obtained by Eq. (21). An interesting behavior of the temperature profile can be seen on Figs. 5 and 6, where the negative temperature gradient is observed: the gas temperature near colder surface becomes higher compared to the temperature near the hotter one. The analogous temperature behaviors were obtained numerically in [42, 50], where the evaporation and condensation were simulated for a single gas. This inverted temperature profile is explained by the significant contribution of the term $\tau_2^P X_{\rm P}$ into the total temperature T containing T_2 calculated by Eq. (22). For larger value of the mole fraction, *i.e.* at $C_0 = 0.9$, the contribution of this term is significantly smaller than that at $C_0 = 0.1$. As a result, the temperature gradient in the gap becomes positive at the large mole fraction. In all cases, the temperature jump is observed near the surfaces which is larger for lower mole fraction of Helium, $C_0 = 0.1$. This jump increases by increasing the rarefaction parameter

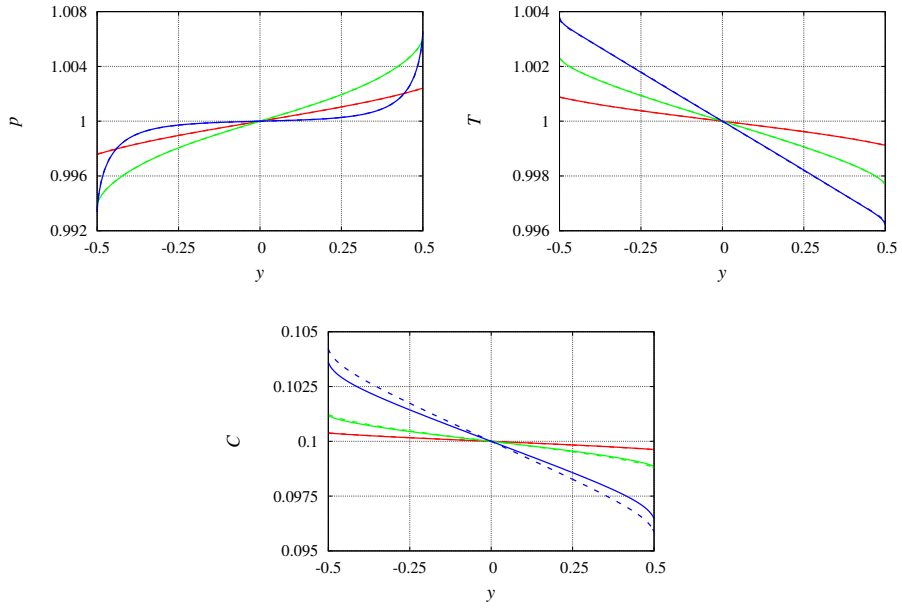

Figure 5: Profiles of pressure p, temperature T, and mole fraction of mixture calculated for the two potentials: solid line - HS, dashed line - AI; red lines - $\delta = 0.1$, green line - $\delta = 1$, blue line - $\delta = 1$; at $C_0 = 0.1$, $T_0 = 50$ K, $X_{\rm P} = 0.083$, and $X_{\rm T} = 0.004$

at $C_0 = 0.1$, while the opposite trend is observed at $C_0 = 0.9$.

The pressure shown in Figs. 5-7 is not constant in the gap. Large pressure gradients are observed near both surfaces for larger value of the rarefaction parameter $\delta = 10$. Like the temperature, the pressure jumps also exist near both surfaces, *i.e.* the gas pressure near the surface is different from the saturation pressure corresponding to the surface temperature. The value of the pressure jump decreases by increasing the Helium mole fraction.

It is worth to underling that the local mole fraction of Helium increases compared to its equilibrium value near the deposition surface, $y = -0.5$, and decreases near the sublimation one, see Figs. 5-7. This increase in the mole fraction, around 1%, is maximal for intermediate, $C_0 = 0.5$ equilibrium mole fraction, and it is larger for the larger rarefaction parameter.

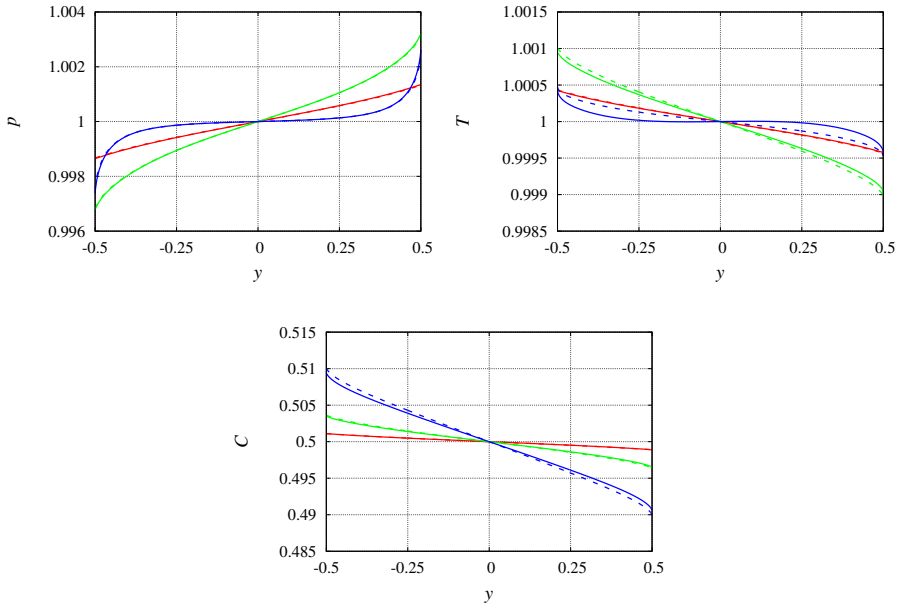

Figure 6: Profiles of pressure p, temperature T, and mole fraction of mixture calculated for the two potentials: solid line - HS, dashed line - AI; red lines - $\delta = 0.1$, green line - $\delta = 1$, blue line - $\delta = 1$; at $C_0 = 0.5$, $T_0 = 50$ K, $X_{\mathrm{P}} = 0.083$, and $X_{\mathrm{T}} = 0.004$

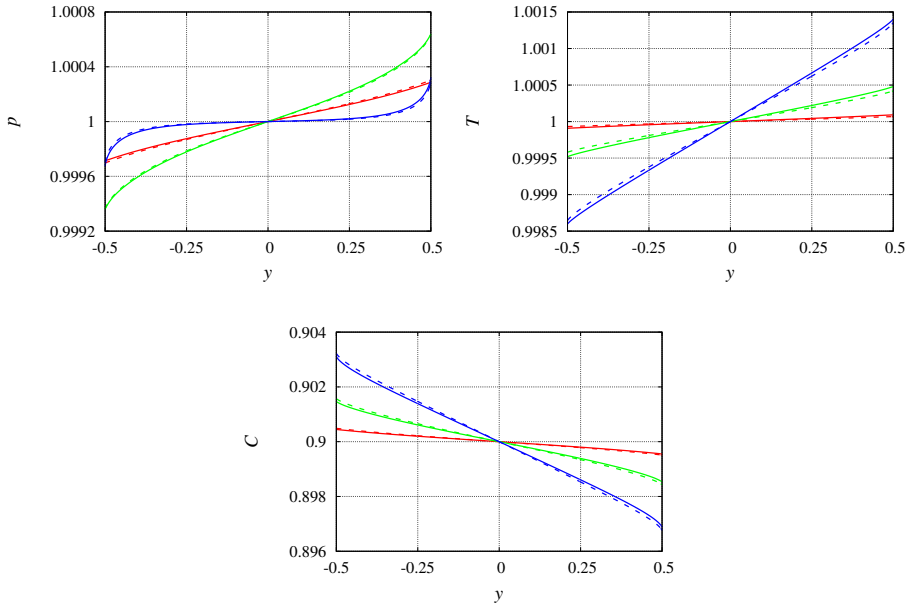

Figure 7: Profiles of pressure p, temperature T, and mole fraction of mixture calculated for the two potentials: solid line - HS, dashed line - AI; red lines - $\delta = 0.1$, green line - $\delta = 1$, blue line - $\delta = 1$; at $C_0 = 0.9$, $T_0 = 50$ K, $X_{\mathrm{P}} = 0.083$, and $X_{\mathrm{T}} = 0.004$

In contrast to the cross kinetic coefficients, the local pressure, temperature and mole fraction are not so sensitive to the potential of intermolecular interaction.

8. Conclusion

The sublimation-deposition process in the Helium-Argon mixture is studied numerically on the basis of the McCormack kinetic equation. The matrix of kinetic coefficients has been calculated for a large range of the rarefaction parameter lying from 0.1 to 20, for three values of the Helium mole fraction $C_0 = 0.1$, 0.5, 0.9, and for two reference temperatures, 50 K and 70 K. In order study the influence of intermolecular potential on macroscopic characteristics, three different potentials, namely, Hard Sphere, Lennard-Jones, and *ab initio*, have been implemented. It was observed that the cross kinetic coefficients, based on the Hard Sphere potential, differ significantly from those obtained for the *ab initio* potential. The discrepancy between coefficients obtained for these two potentials reach 100%. The diagonal kinetic coefficients are less sensitive to the potential. In this case, the potential influence is about 17%. At the same time, the local characteristics, such as pressure, temperature and mole fraction, are weakly sensitive to the intermolecular potential. All kinetic coefficients based on the Lennard-Jones potential just slightly differ from the corresponding coefficients based on the *ab initio* potentail. Thus, the Lannrd-Jones potential with parameters calculated *ab initio* provides reliable results as well as the *ab initio* potential itself.

Using the numerical data on the kinetic coefficients, the sublimation rate and the heat flux through the mixture have been calculated assuming the relative temperature difference equal to 0.004. The relative pressure difference of Argon has been calculated using the experimental relation provided in Ref. [23]. It

has been found that the absolute value of the sublimation rate decreases by increasing the rarefaction parameter and it decreases considerably by increasing of the non-condensable gas (Helium) equilibrium concentration. The heat flux through the gap changes its direction depending on the Helium mole fraction: for its small value, $C_0 = 0.1$, the heat flows from the cold surface to the hot one, while it flows in the opposite direction at $C_0 = 0.9$. The total energy flux always directed from the hot plate to the cold one.

Interesting effect, of the negative temperature gradient, where the gas temperature near the colder surface becomes larger than that near the hotter surface is observed for $C_0 = 0.1$ and 0.5. This phenomenon called inverted temperature profile was found previously in the numerical modeling of the evaporation and condensation phenomena, see Refs. [42, 50, 43].

Finally, the original approach has been developed to simulate the sublimation and deposition phenomena in the gap between two solid surfaces filled by a mixture of condensable and non-condensable gases. These results could be used to model gas flows at cryogenic temperatures.

Appendix A. Collision term

Expression of the collisional term of Eq. (12):

$$\begin{aligned}\hat{L}_{\alpha\beta}h^{(i)} = &-\gamma_{\alpha\beta}h_{\alpha}^{(i)}+\gamma_{\alpha\beta}\nu_{\alpha}^{(i)}\\ &+2\sqrt{\frac{m_\alpha}{m}}\left[\gamma_{\alpha\beta}u_{\alpha}^{(i)}-\upsilon_{\alpha\beta}^{(1)}\left(u_{\alpha}^{(i)}-u_{\beta}^{(i)}\right)-\frac{\upsilon_{\alpha\beta}^{(2)}}{2}\left(q_{\alpha}^{(i)}-\frac{m_\alpha}{m_\beta}q_{\beta}^{(i)}\right)\right]c_{\alpha y}\\ &+\left[\gamma_{\alpha\beta}\tau_{\alpha}^{(i)}-\frac{2m_\alpha}{m_\alpha+m_\beta}\left(\tau_{\alpha}^{(i)}-\tau_{\beta}^{(i)}\right)\upsilon_{\alpha\beta}^{(1)}\right]\left(c_\alpha^2-\frac{3}{2}\right)\\ &+2\left[\left(\gamma_{\alpha\beta}-\upsilon_{\alpha\beta}^{(3)}\right)\Pi_{\alpha}^{(i)}+\upsilon_{\alpha\beta}^{(4)}\Pi_{\beta}^{(i)}\right]\left(c_{\alpha y}^2-\frac{1}{2}c_{\alpha x}^2-\frac{1}{2}c_{\alpha z}^2\right)\\ &+\frac{4}{5}\sqrt{\frac{m_\alpha}{m}}\left[\left(\gamma_{\alpha\beta}-\upsilon_{\alpha\beta}^{(5)}\right)q_{\alpha}^{(i)}+\upsilon_{\alpha\beta}^{(6)}\sqrt{\frac{m_\beta}{m_\alpha}}q_{\beta}^{(i)}\right.\\ &\left.-\frac{5}{4}\upsilon_{\alpha\beta}^{(2)}\left(u_{\alpha}^{(i)}-u_{\beta}^{(i)}\right)\right]c_{\alpha y}\left(c_\alpha^2-\frac{5}{2}\right).\end{aligned}$$

(A.1)

where $\alpha, \beta = 1, 2$, and $\upsilon_{\alpha\beta}^{(i)}$ are defined as following

$$
\begin{aligned}
\upsilon_{\alpha\beta}^{(1)} &= \frac{16}{3}\frac{m_{\alpha\beta}}{m_\alpha} n_\beta \Omega_{\alpha\beta}^{11}, \\
\upsilon_{\alpha\beta}^{(2)} &= \frac{64}{15}\left(\frac{m_{\alpha\beta}}{m_\alpha}\right)^2 n_\beta \left[\Omega_{\alpha\beta}^{12} - \frac{5}{2}\Omega_{\alpha\beta}^{11}\right], \\
\upsilon_{\alpha\beta}^{(3)} &= \frac{16}{5}\frac{m_{\alpha\beta}^2}{m_\alpha m_\beta} n_\beta \left[\frac{10}{3}\Omega_{\alpha\beta}^{11} + \frac{m_\beta}{m_\alpha}\Omega_{\alpha\beta}^{22}\right], \\
\upsilon_{\alpha\beta}^{(4)} &= \frac{16}{5}\frac{m_{\alpha\beta}^2}{m_\alpha m_\beta} n_\beta \left[\frac{10}{3}\Omega_{\alpha\beta}^{11} - \Omega_{\alpha\beta}^{22}\right], \\
\upsilon_{\alpha\beta}^{(5)} &= \frac{64}{15}\left(\frac{m_{\alpha\beta}}{m_\alpha}\right)^3 \frac{m_\alpha}{m_\beta} n_\beta \left[\Omega_{\alpha\beta}^{22} + \left(\frac{15}{4}\frac{m_\alpha}{m_\beta} + \frac{25}{8}\frac{m_\beta}{m_\alpha}\right)\Omega_{\alpha\beta}^{11} - \frac{1}{2}\frac{m_\beta}{m_\alpha}\left(5\Omega_{\alpha\beta}^{12} - \Omega_{\alpha\beta}^{13}\right)\right], \\
\upsilon_{\alpha\beta}^{(6)} &= \frac{64}{15}\left(\frac{m_{\alpha\beta}}{m_\alpha}\right)^3 \left(\frac{m_\alpha}{m_\beta}\right)^{3/2} n_\beta \left[-\Omega_{\alpha\beta}^{22} + \frac{55}{8}\Omega_{\alpha\beta}^{11} - \frac{5}{2}\Omega_{\alpha\beta}^{12} + \frac{1}{2}\Omega_{\alpha\beta}^{13}\right],
\end{aligned}
\tag{A.2}
$$

where

$$
m_{\alpha\beta} = \frac{m_\alpha m_\beta}{m_\alpha + m_\beta} \tag{A.3}
$$

is the reduced mass of the binary mixture. The Ω integrals are defined via the differential cross section σ as

$$
\Omega_{\alpha\beta}^{(i,j)}(T) = \sqrt{\frac{\pi k_\mathrm{B} T}{2 m_{\alpha\beta}}} \int_0^\infty \int_0^\pi \left(1 - \cos^i \chi\right) \sigma(\mathcal{E}, \chi) \sin\chi \mathcal{E}^{j+1} e^{-\mathcal{E}} \mathrm{d}\chi \mathrm{d}\mathcal{E}, \tag{A.4}
$$

where $\mathcal{E}$ is the dimensionless energy of colliding particles

$$
\mathcal{E} = \frac{m_{\alpha\beta} |\boldsymbol{v}_\alpha - \boldsymbol{v}_\beta|^2}{2 k_\mathrm{B} T}. \tag{A.5}
$$

The dependence of the differential cross section σ on the energy $\mathcal{E}$ and deflection angle χ is determined by the potential of interatomic potential. In case of *ab initio* and Lennard-Jones potentials, the quantity $\sigma(\mathcal{E}, \chi)$ is calculated numerically using the quantum theory to interatomic collision [24, 51]. Then, the Ω

integral is calculated numerically for each value of the temperature. For HS potential, the Ω integral is calculated analytically and reads [26]

$$\Omega_{\alpha\beta}^{(i,j)} = \frac{(j+1)!}{8}\left[1 - \frac{1+(-1)^i}{2(i+1)}\right]\sqrt{\frac{\pi k_{\mathrm{B}} T}{2m_{\alpha\beta}}}\left(d_\alpha + d_\beta\right)^2. \tag{A.6}$$

Appendix B. Sublimation pressure

The saturation pressure, p_s/Pa, as function of the temperature T/K, is calculated using the following equation, [23]:

$$\ln p_s = A - \frac{B}{T} + C\ln T + \sum_{i=2}^{4} D_i T^{i-1} + E(T)p_s/T, \tag{B.1}$$

where $A = 10.9131$, $B = 930.108$, $C = 3.7667$, $D_2 = -9.5811 \times 10^{-2}$, $D_3 = 5.0314 \times 10^{-4}$, $D_4 = 15.081 \times 10^{-7}$,

$$E(T)/T = E_1 + E_2\,T + E_3/T + E_4/T^2 + E_5/T^3, \tag{B.2}$$

with $E_1 = 0.5361 \times 10^{-10}$, $E_2 = 3.6255 \times 10^{-11}$, $E_3 = 3.1971 \times 10^{-6}$, $E_4 = 1.0422 \times 10^{-4}$, $E_5 = 0.2084$.

Acknowledgements

The work of A. Polikarpov was financially supported by the Ministry of Science and Higher Education of the Russian Federation, the research project No FEUZ-2020-0057. I. Graur would like to acknowledge the financial support provided by the European Union network program H2020, MIGRATE project under Grant Agreement No.643095. F. Sharipov acknowledges the Brazilian Agency CNPq for the support of his research, grant 304831/2018-2.

[1] A. Hachikubo, Numerical modelling of sublimation on snow and comparison with field measurements, Annals of Glaciology 32 (2001) 27–32.

[2] V. Vionnet, E. Martin, V. Masson, G. Guyomarc'h, F. Naaim-Bouvet, A. Prokop, Y. Durand, C. Lac, Simulation of wind-induced snow transport and sublimation in alpine terrain using a fully coupled snowpack/atmosphere model, The Cryosphere 8 (2014) 395–415.

[3] C. M. Dundas, S. Byrne, Modeling sublimation of ice exposed by new impacts in the martian mid-latitudes, Icarus 206 (2010) 716–728.

[4] J. F. Crifo, Improved gas-kinetic treatment of cometary water sublimation and recondensation: application to coment P/Halley, Astron. Astrophys. 187 (1987) 438–450.

[5] Y. V. Skorov, N. I. Kömle, H. U. Keller, G. Kargl, W. J. Markiewicz, A model of heat and mass transfer in a porous cometary nucleus based on a kinetic treatment of mass flow, Icarus 153 (2001) 180–196.

[6] Y. V. Skorov, G. N. Markelov, H. U. Keller, Direct statistical simulation of the near-surface layers of the cometary atmosphere. I. A spherical nucleus, Solar System Research 38 (6) (2004) 455–475.

[7] I. Igumenov, M. Makarov, S. Makarova, Heat and mass transfer at sublimation of a single chromium (iii) and zirconium (iv) beta-diketonate particle in the inert gas mixture, in: MATEC Web of Conferences 115, no. 08001 in STS-33, 2017.

[8] H.-Y. Tung, Z.-Y. Guan, T.-Y. Liu, H.-Y. Chen, Vapor sublimation and deposition to build porous particles and composites, Nature communications 9 (2564) (2018) 1–8.

[9] J. Xiang, J. M. Hey, V. Liedtke, D. Q. Wang, Investigation of freeze–drying

sublimation rates using a freeze–drying microbalance technique, International Journal of Pharmaceutics 279 (2004) 95–105.

[10] I. Oddone, A. A. Barresi, R. Pisano, Influence of controlled ice nucleation on the freeze-drying of pharmaceutical products: the secondary drying step, International Journal of Pharmaceutics 524 (2017) 134–140.

[11] Y. Sone, Molecular Gas Dynamics, Birkhäuser, Boston, 2007.

[12] B. B. Hamel, Kinetic model for binary gas mixture, Phys. Fluids 8 (3) (1965) 418–425.

[13] Y. Onishi, The spherical-droplet problem of evaporation and condensation in a vapour-gas mixture, Journal of Fluid Mechanics 163 (171-194).

[14] V. Garzó, A. Santos, J. J. Brey, A kinetic model for a multicomponent gas, Phys. Fluids A 1 (2) (1989) 380–383.

[15] Y. Sone, K. Aoki, T. Doi, Kinetic theory analysis of gas flows condensing on a plane condensed phase: case of a mixture of a vapor and a noncondensable gas, Transp. Theory Stat. Phys. 21 (1992) 297–328.

[16] S. Kosuge, Model Boltzmann equation for gas mixtures: Construction and numerical comparison, Eur. J. Mech. B/Fluids 28 (2009) 170–184.

[17] K. Aoki, S. Takata, S. Kosuge, Vapor flows caused by evaporation and condensation on two parallel plane surfaces: Effect of the presence of a noncondensable gas, Phys. of Fluids 10 (6) (1998) 1519–1533.

[18] S. Taguchi, K. Aoki, V. Latocha, Vapor flows along a plane condensed phase with weak condensation in the presence of a noncondensable gas, Journal of Statistical Physics 124 (2-4) (2006) 321–369.

[19] S. Taguchi, K. Aoki, S. Takata, Vapor flows in the continuum limit in the presence of a small amount of noncondensable gas, Physic of Fluids 16 (11) (2004) 4105–4120.

[20] H. Yoshida, K. Aoki, Cilindrical Couette flow of a vapor-gas mixture: Ghost effect and bifurcation in the continuum limite, Physic of Fluids 18 (087103).

[21] V. G. Chernyak, The kinetic theory of droplet evaporation, J. Aerosol Science 26 (6) (1995) 873–885.

[22] K. Aoki, S. Takata, S. Taguchi, Vapor flows with evaporation and condensation in the continuum limit: effect of a trace of noncondensable gas, Europeen Journal of Mechanics/B Fluids 22 (2003) 51–71.

[23] A. G. M. Ferreira, L. Q. Lobo, The sublimation of argon, krypton, and xenon, J.Chem.Thermodynamics 40 (1621-1626).

[24] F. Sharipov, V. Benites, Transport coefficients of argon and its mixtures with helium and neon at low density based *ab initio* potentials, Fluid Phase Equilibria 498 (2019) 23–32.

[25] F. Sharipov, Rarefied Gas Dynamics. Fundamentals for Research and Practice, Wiley-VCH, Berlin, 2016.

[26] J. H. Ferziger, H. G. Kaper, Mathematical Theory of Transport Processes in Gases, North-Holland Publishing Company, Amsterdam, 1972.

[27] F. Sharipov, G. Bertoldo, Poiseuille flow and thermal creep based on the Boltzmann equation with the Lennard-Jones potential over a wide range of the Knudsen number, Phys. Fluids 21 (2009) 067101.

[28] O. I. Dodulad, Y. Y. Kloss, D. O. Savichkin, F. G. Tcheremissine, Knudsen pumps modeling with Lennard-Jones and ab initio intermolecular potentials, Vacuum 109 (2014) 360–367.

[29] W. Su, P. Wang, H. Liu, L. Wu, Accurate and efficient computation of the Boltzmann equation for Couette flow: Influence of intermolecular potentials on Knudsen layer function and viscous slip coefficient, J. Comp. Phys. 378 (2019) 573–590. doi:https://doi.org/10.1016/j.jcp.2018.11.015.

[30] F. Sharipov, J. L. Strapasson, Benchmark problems for mixtures of rarefied gases. I. Couette flow, Phys. Fluids 25 (2013) 027101.

[31] J. L. Strapasson, F. Sharipov, *Ab initio* simulation of heat transfer through a mixture of rarefied gases, Int. J. Heat Mass Transfer 71 (2014) 91–97.

[32] M. T. Ho, L. Wu, I. Graur, Y. Zhang, R. J. M, Comparative study of the Boltzmann and McCormack equations for Couette and Fourier flows of binary gaseous mixtures, Int. J. Heat Mass Transfer 96 (2016) 29–41.

[33] F. J. McCormack, Construction of linearized kinetic models for gaseous mixture and molecular gases, Phys. Fluids 16 (1973) 2095–2105.

[34] E. M. Shakhov, Generalization of the Krook kinetic relaxation equation, Fluid Dyn. 3 (5) (1968) 95–96.

[35] F. Sharipov, D. Kalempa, Gaseous mixture flow through a long tube at arbitrary Knudsen number, J. Vac. Sci. Technol. A 20 (3) (2002) 814–822.

[36] F. Sharipov, L. M. G. Cumin, D. Kalempa, Plane Couette flow of binary gaseous mixture in the whole range of the Knudsen number, Eur. J. Mech. B/Fluids 23 (2004) 899–906.

[37] A. P. Polikarpov, M. T. Ho, I. Graur, Transient heat transfer in a rarefied binary gas mixture confined between parallel plates due to a sudden small change of wall temperatures, International Journal of Heat and Mass Transfer 101 (2016) 1292–1303.

[38] F. Sharipov, Onsager-Casimir reciprocity relations for open gaseous systems at arbitrary rarefaction. III. Theory and its application for gaseous mixtures, Physica A 209 (1994) 457–476.

[39] A. Polikarpov, I. Graur, Unsteady rarefied gas flow through a slit, Vacuum 101 (2014) 79 – 85. doi:http://dx.doi.org/10.1016/j.vacuum.2013.07.006.

[40] R. Courant, K. Friedrichs, H. Lewy, On the partial difference equations of mathematicalphysics, IBM Journal on Research and development 11 (2) (1967) 215–234.

[41] I. A. Graur, A. Polikarpov, Comparison of different kinetic models for the heat transfer problem, Heat and Mass Transfer 46 (2009) 237–244.

[42] K. Aoki, N. Masukawa, Gas flows caused by evaporation and condensation on two parallel condensed phases and the negative temperature gradient: numerical analysis by using a nonlinear kinetic equation, Phys. Fluids 6 (3) (1994) 1379–1395.

[43] A. Polikarpov, I. Graur, Heat and mass transfer in a rarefied gas confined between its two parallel condensed phases, Int. J. Heat Mass Transfer 124 (2018) 967–979.

[44] F. Sharipov, L. M. G. Cumin, D. Kalempa, Heat flux through a binary gaseous mixture over the whole range of the knudsen number, Physica A 378 (2007) 183–193.

[45] E. Bich, R. Hellmann, E. Vogel, Ab initio potential energy curve for the helium atom pair and thermophysical properties of the dilute helium gas. II. Thermophysical standard values for low-density helium, Mol. Phys. 105 (2007) 3035–3049.

[46] F. Sharipov, M. R. Moldover, Energy accommodation coefficient extracted from acoustic resonator experiments, J. Vac Sci. Technol. A 34 (6).

[47] W. Cencek, M. Przybytek, J. Komasa, J. B. Mehl, B. Jeziorski, K. Szalewicz, Effects of adiabatic, relativistic, and quantum electrodynamics interactions on the pair potencial and thermophysical properties of helium, J. Chem. Phys. 136 (22) (2012) 224303.

[48] K. Patkowski, K. Szalewicz, Argon pair potential at basis set and excitation limits, J. Chem. Phys. 133 (2010) 094304.

[49] J. Cacheiro, B. Fernández, D. Marchesan, S. Coriani, C. Hättig, A. Rizzo, Coupled cluster calculations of the ground state potential and interaction induced electric properties of the mixed dimers of helium, neon and argon, Mol. Phys. 102 (2004) 101–110.

[50] C. Cercignani, W. Fiszdon, A. Frezzotti, The paradox of the inverted temperature profiles between an evaporating and a condensing surface, Phys. Fluids 28 (11) (1985) 3237–3240.

[51] F. Sharipov, V. Benites, Transport coefficients of helium-neon mixtures at low density computed from Ab initio potentials, J. Chem. Phys. 147 (2017) 224302.